

Rising Extreme Meltwater Trends in Greenland Ice Sheet (1950–2022): Surface Energy Balance and Large-Scale Circulation Changes

JOSEP BONSONS ^a, MARC OLIVA,^a JUAN I. LÓPEZ-MORENO,^b AND XAVIER FETTWEIS^c

^a *Department of Geography, Universitat de Barcelona, Barcelona, Spain*

^b *Instituto Pirenaico de Ecología (CSIC), Campus de Aula Dei, Zaragoza, Spain*

^c *Department of Geography, SPHERES Research Unit, University of Liège, Liège, Belgium*

(Manuscript received 30 June 2023, in final form 29 April 2024, accepted 9 June 2024)

ABSTRACT: The Greenland Ice Sheet (GrIS) meltwater runoff has increased considerably since the 1990s, leading to implications for the ice sheet mass balance and ecosystem dynamics in ice-free areas. Extreme weather events will likely continue to occur in the coming decades. Therefore, a more thorough understanding of the spatiotemporal patterns of extreme melting events is of interest. This study aims to analyze the evolution of extreme melting events across the GrIS and determine the climatic factors that drive them. Specifically, we have analyzed extreme melting events (90th percentile) across the GrIS from 1950 to 2022 and examined their links to the surface energy balance (SEB) and large-scale atmospheric circulation. Extreme melting days account for approximately 35%–40% of the total accumulated melting per season. We found that extreme melting frequency, intensity, and contribution to the total accumulated June–August (summer) melting show a statistically significant upward trend at a 95% confidence level. The largest trends are detected across the northern GrIS. The trends are independent of the extreme melting percentile rank (90th, 97th, or 99th) analyzed and are consistent with average melting trends that exhibit an increase in similar magnitude and spatial configuration. Radiation plays a dominant role in controlling the SEB during extreme melting days. The increase in extreme melting frequency and intensity is driven by the increase in anticyclonic weather types during summer and more energy available for melting. Our results help to enhance the understanding of extreme events in the Arctic.


KEYWORDS: Ice sheets; Atmospheric circulation; Climate; Surface fluxes; Regional models


1. Introduction

Arctic temperatures are increasing faster than the global mean since the 1990s (Rantanen et al. 2022). Consequently, Northern Hemisphere snow and ice mass are decreasing (Mudryk et al. 2020; Pulliainen et al. 2020; IPCC 2022). The Greenland Ice Sheet (GrIS) is largely affected by Arctic amplification (Serreze and Barry 2011) and is undergoing a fast retreat since the 1990s (IPCC 2022; Mouginot et al. 2019). Mid-to-end twenty-first-century high-emission climate projections for high latitudes indicate snowfall increases (Räisänen 2008; Krasting et al. 2013; Brutel-Vuilmet et al. 2013), although it will not counterbalance the anticipated GrIS summer melting (Vizcaíno et al. 2014) and the associated increase in runoff (Noël et al. 2019). High-emission CMIP6 scenarios suggest that the surface mass balance from 1961 to 2100 will contribute approximately 17.8 ± 7.8 cm to global sea level rise (Hofer et al. 2017). GrIS-increased melting trends have relevant impacts on surrounding areas, such as enhancing snow line migration (Ryan et al. 2019), leading to albedo

decay (Tedesco et al. 2011) and lake formation (How et al. 2021), affecting shoreline ecological and permafrost dynamics (IPCC 2022). Further, GrIS meltwater runoff is one of the largest projected sea level rise contributions (Hofer et al. 2017) and could alter global ecosystems by changing oceanic circulation dynamics (Rahmstorf et al. 2015). Given that GrIS meltwater runoff is responsible for approximately 50% of the GrIS recent mass loss (van den Broeke et al. 2008), a better understanding of their climate and environmental drivers and recent trends is of major importance.

Prior studies have examined the prevailing synoptic conditions in GrIS and its relation with melting (Mote 1998; Fettweis et al. 2011a; Mioduszewski et al. 2016) and mass balance at Summit Station, Greenland (Gallagher et al. 2020). Additionally, other research has analyzed the SEB partitioning during melting (Mattingly et al. 2018; Hermann et al. 2020), atmospheric rivers (Mattingly et al. 2020), and omega-blocking events (Preece et al. 2023). The upward trends in temperature, meltwater runoff, and ice flow detected in GrIS since the 1990s from different data and method sources (Slater et al. 2021; Mote 2007; Box 2013; Fettweis et al. 2013, 2017, 2011a; Hanna et al. 2012; Wilton et al. 2017; Hanna et al. 2011) have been mostly driven by atmospheric circulation weather type (CWT) variability (Fettweis et al. 2011a). CWTs play a key role in controlling clouds (Ward et al. 2020), moisture advection (Mattingly et al. 2016; Oltmanns et al. 2019), and surface energy balance (SEB) partitioning (Fausto et al. 2016; Huai et al. 2020), which ultimately drive melting patterns of GrIS (Fettweis et al. 2011a; Häkkinen et al. 2014; Mioduszewski et al. 2016; Cullather and Nowicki 2018; Välisuo et al. 2018). The positive meltwater and

 Denotes content that is immediately available upon publication as open access.

 Supplemental information related to this paper is available at the Journals Online website: <https://doi.org/10.1175/JCLI-D-23-0396.s1>.

Corresponding author: Josep Bonsoms, josepbonsoms5@ub.edu

DOI: 10.1175/JCLI-D-23-0396.1

© 2024 American Meteorological Society. This published article is licensed under the terms of the default AMS reuse license. For information regarding reuse of this content and general copyright information, consult the AMS Copyright Policy (www.ametsoc.org/PUBSReuseLicenses).

runoff anomalies since the 1990s have been attributed to the increase in anticyclonic events (Fettweis et al. 2011a; Rajewicz and Marshall 2014) and anticyclonic omega-block-type evolution (Preece et al. 2023), which are linked to the negative summer phase of the North Atlantic Oscillation (NAO) (Hanna et al. 2013) and positive phases of Greenland blocking index (GBI) (Hanna et al. 2018) and Atlantic multidecadal oscillation (AMO) (McLeod and Mote 2016). Furthermore, the energy available for melting has increased across GrIS regardless of the synoptic configuration (Mioduszewski et al. 2016).

Extreme negative surface mass balance (SMB) events show an increase for most GrIS areas during the two recent decades (2001–19 period) (Wei et al. 2022). Future climate change could promote more extreme weather events (Francis and Vavrus 2012; IPCC 2022). These episodes promote extreme melting events in GrIS, such as in July 2012, which was unprecedented in satellite and instrumental records (Nghiem et al. 2012) and extremely rare in long-term paleoclimate observations (Alley and Anandakrishnan 1995). Several studies have analyzed SEB partitioning and melt during the extreme melt event in 2012 (Fausto et al. 2016) and 2021 (Box et al. 2022), as well as the atmospheric circulation drivers of melting for extreme events in 2007 (Tedesco et al. 2008), 2012 (Tedesco et al. 2013), and 2019 (Tedesco and Fettweis 2020). In the 2012 event, the cumulative low albedo recorded in GrIS during the previous years enhanced extreme melting (Hanna et al. 2012), along with snow and ice black carbon deposition (Keegan et al. 2014), and radiative heat flux anomalies induced by low-level clouds (Bennartz et al. 2013; Van Tricht et al. 2016). Extreme melting largely reduces the albedo (Tedesco et al. 2016) and promotes glacial retreat that exposes ice-free environment exposure (Box et al. 2012). Extreme melting leads to substantial impacts on firn refreezing (de la Peña et al. 2015) and on meltwater capacity retention (MacFerrin et al. 2019), with major impacts on ice sheet stability and water infiltration in subsequent years (Culberg et al. 2021).

The focus of this study is to analyze the spatiotemporal patterns of extreme melting in GrIS from 1950 to 2022 and its impact on the total accumulated summer melting. We further examine the link between CWTs and the SEB partitioning during days of extreme melting, providing a comprehensive overview of the thermodynamic and dynamic drivers influencing the recent long-term trends in extreme GrIS meltwater. The following specific questions are addressed:

- (i) What are the spatiotemporal patterns and trends of extreme melting events, their frequency, and intensity in GrIS?
- (ii) What is the SEB partitioning during extreme melting days?
- (iii) Which CWTs are responsible for driving extreme melting episodes in GrIS?

2. Data and methods

This work focuses on melting, extreme melting, and the SEB during these events. We analyzed the role of SEB variables related to melting, including net shortwave radiation

(SWnet), net longwave radiation (LWnet), sensible heat flux (SHF), and latent heat flux (LHF). SWnet is calculated by multiplying downward shortwave radiation (SWD) by 1 minus albedo. LWnet is calculated as the difference between downward longwave radiation (LWD) and upward longwave radiation (LWU). The SEB contribution to extreme melting is calculated at pixel scale by summing the positive energy from the SEB components during extreme melting events, dividing this sum by the total positive energy, and multiplying by 100. We also analyzed cloud-cover conditions for each synoptic situation, including cloud-cover anomalies at the down level (CD) with pressures >680 hPa and at the up level (CU) with pressures <440 hPa. The atmospheric and surface variables included were simulated with the mesoscale atmospheric model Modèle Atmosphérique Régional version 3.13 (MAR v3.13) run at a resolution of 10 km (Fettweis et al. 2020). MAR v3.13 is a hydrostatic atmospheric model that solves the prognostic meteorological equations, including cloud microphysical model (Gallée and Schayes 1994). MAR v3.13 is coupled with the multilayer one-dimensional energy balance soil–ice–snow–vegetation–atmosphere transfer (SISVAT) model (De Ridder and Gallé 1998). MAR v3.13 melting is simulated through the snow and ice SISVAT module based on the CROCUS model. CROCUS is a one-dimensional multilayer model that simulates the energy and mass balance of the snowpack, including snow densification and metamorphism, albedo decay, snow and ice discretization, and meltwater refreezing (Brun et al. 1992). MAR v3.13 was 6 hourly forced by the ERA5 reanalysis (Hersbach et al. 2020). ERA5 has a vertical resolution of 137 pressure levels and a spatial resolution of 0.3° (ca. 15 km at GrIS). ERA5 is based on a 4D-Var system based on the Integrated Forecasting System, which assimilates in situ records. MAR v3.13 has been extensively validated in GrIS against in situ, passive microwave remote sensing data and other regional climate models (i.e., Fettweis et al. 2011b, 2013, 2020). Delhasse et al. (2020) conducted a comprehensive evaluation of near-surface climate variables in GrIS by comparing independent (not data assimilated) Programme for Monitoring of the Greenland Ice Sheet (PROMICE) network observations, against the ERA5, ERA-Interim, Arctic System Reanalysis, and the regional climate model MAR forced with ERA5. The study reported the accurate performance of MAR v3.13 forced with ERA5 with reliable temperature, wind, and radiative heat flux estimation. Finally, with respect to the version 3.12 of MAR used in Antwerpen et al. (2022) to simulate melt and albedo, in addition to the usual small bug corrections and computer time improvements, version 3.13 is only a rewriting of the FORTRAN MAR code.

We focused our study on GrIS sectors defined by Rignot and Mouginot (2012) and determined based on their geographical position and characteristics such as size, ice flow, and runoff production.

a. Melting indicators

We have conducted an analysis of GrIS melting episodes during summer (June–August, included) over a period spanning

from 1950 to 2022 (both years included). Following Fausto et al. (2016) and Franco et al. (2013), we determined a melting day when produced meltwater was ≥ 1 mmWE day⁻¹. Extreme melting was determined through a percentile approach at a grid scale. We subtracted the 90th-percentile value of melting days for the 20 years of reference period 1986 to 2005 (both years included). The reference period is in accordance with previous extreme GrIS SMB studies (Wei et al. 2022), which is consistent with the IPCC-AR6 reference period in polar regions (Constable et al. 2022). To better understand the spatial distribution of extreme melting events across different sectors of GrIS, we computed the average number of melting days for each GrIS sector. The indicators that we have included in our study are as follows:

- (i) Accumulated summer melting (ME)
- (ii) Number of melting days per season (dME)
- (iii) Accumulated summer extreme melting (>90th percentile) per season M
- (iv) Number of summer extreme melting days per season (dME90)
- (v) Contribution of ME90 to ME (CE90)

We have also explored differences between extreme melting days considering different percentile ranks, namely, for the 97th (dME97) and 99th (dME99) percentiles, as well as the accumulated melting during summer for dME97 (ME97) and dME99 (ME99) days. This approach allows us to investigate the influence of percentile selection more comprehensively on extreme melting events.

b. Trend analysis

To evaluate trends, we employed least squares regression, the Mann–Kendall trend test (Kendall 1949), and Sen's slope (Sen 1968). The Mann–Kendall trend test and Sen's slope are widely used nonparametric methods for identifying temporal trends. These methods are included in the manuscript due to their low sensitivity to outliers and the absence of assumptions regarding data distributions (Kendall 1949; Sen 1968).

c. Circulation weather type classification

We classified the prevailing CWTs during summer across GrIS using an automated synoptic classification method described by Esteban et al. (2005). This is an objective and standardized method for grouping similar synoptic configurations, distinguishing between distinct groups. The method was compared and validated in the European COST733 project (Philipp et al. 2016). This classification method has been used previously to analyze snowfall (Esteban et al. 2005), snow accumulation (Bonsoms et al. 2021), and CWT characterization of snow ablation events (Bonsoms et al. 2022), among other works. Atmospheric circulation across Greenland was captured through the application of a CWT based on daily 500-hPa geopotential height (Z500) from 50°–90°N to 100°W–10°E. Data are obtained from NCEP–NCARv1 (Kalnay et al. 2018) following previous synoptic classification of melting over GrIS (Fettweis et al. 2011a), extreme melting events (Tedesco and Fettweis 2020), and GBI analysis (Hanna et al. 2012, 2016). The CWT

based on Z500 is preferred over sea level pressure for analyzing surface melt in GrIS because of the ice sheet maximum elevation (3250 m) and because anticyclonic conditions are generally more relevant than flow direction (Fettweis et al. 2011a). The CWT classification was applied using the synoptReg R package (Lemus-Canovas et al. 2019). The main steps of the CWT classification method are as follows: (i) A principal component analysis (PCA) is performed over daily summer Z500 data to retain most of the Z500 variability. The explained variance of each PC can be found in Fig. S1 in the online supplemental material. Subsequently, (ii) a K-means clustering method with S-mode matrix and varimax rotation is performed over the retained PCs. Each PC results in two CWTs, given that the CWTs are determined by the minimum and maximum positive and negative correlation.

3. Results

We examined the dME90, ME90, and CE90 temporal trends and spatial patterns in GrIS between 1950 and 2022. Subsequently, we analyzed the SEB partitioning during dME90 days and conducted a synoptic characterization of extreme melting events in GrIS, by analyzing the CWTs prevailing during these events.

a. Melting intensity

The temporal evolution of ME90 is shown in Figs. 1–3. A general increase in ME90 is simulated, which is consistent with the upward ME trend (Fig. S2). There are no relevant differences in the percentile rank (90th, 97th, and 99th) used for the definition of extreme melting episodes, and most indicators suggest similar temporal trends (Figs. S2–S4). In addition, trends derived from least squares regression values and Mann–Kendall trend analysis exhibit consistency (Figs. 1–3). The largest trends of ME90 are evident for the northern sectors, specifically in northwest (NW) [τ Mann–Kendall (MK) = 0.32; p value < 0.01], northeast (NE) (τ MK = 0.30; p value < 0.01), and northern (N) GrIS (τ MK = 0.30; p value < 0.01). During recent decades, CE90 has accounted for approximately 40% of the total accumulated summer melting and displays low variability across sectors (Fig. 1). In detail, NW (τ MK = 0.30; p value < 0.01) and N (τ MK = 0.30; p value < 0.01) show a remarkable increase in CE90, which is higher than that simulated in other sectors. The most important changes in ME occur in NE and southeast (SE) (Figs. 2 and 3). These trends are statistically significant at the 99% level across the near coastal areas of GrIS (Fig. 2) and long-term periods (Fig. 3). However, some indicators show temporal variability, with changing trends at short-term scales. For instance, a nonstatistically significant downward trend in ME and ME90 is simulated across the northern GrIS during the most recent decades (Fig. 3), which contrasts with the evolution simulated during the 1950–2022 period.

b. Melting frequency

The temporal evolution of dME90 and dME in Greenland has undergone a general increase since the 1990s (Figs. 1 and 2), with only minor differences observed for periods

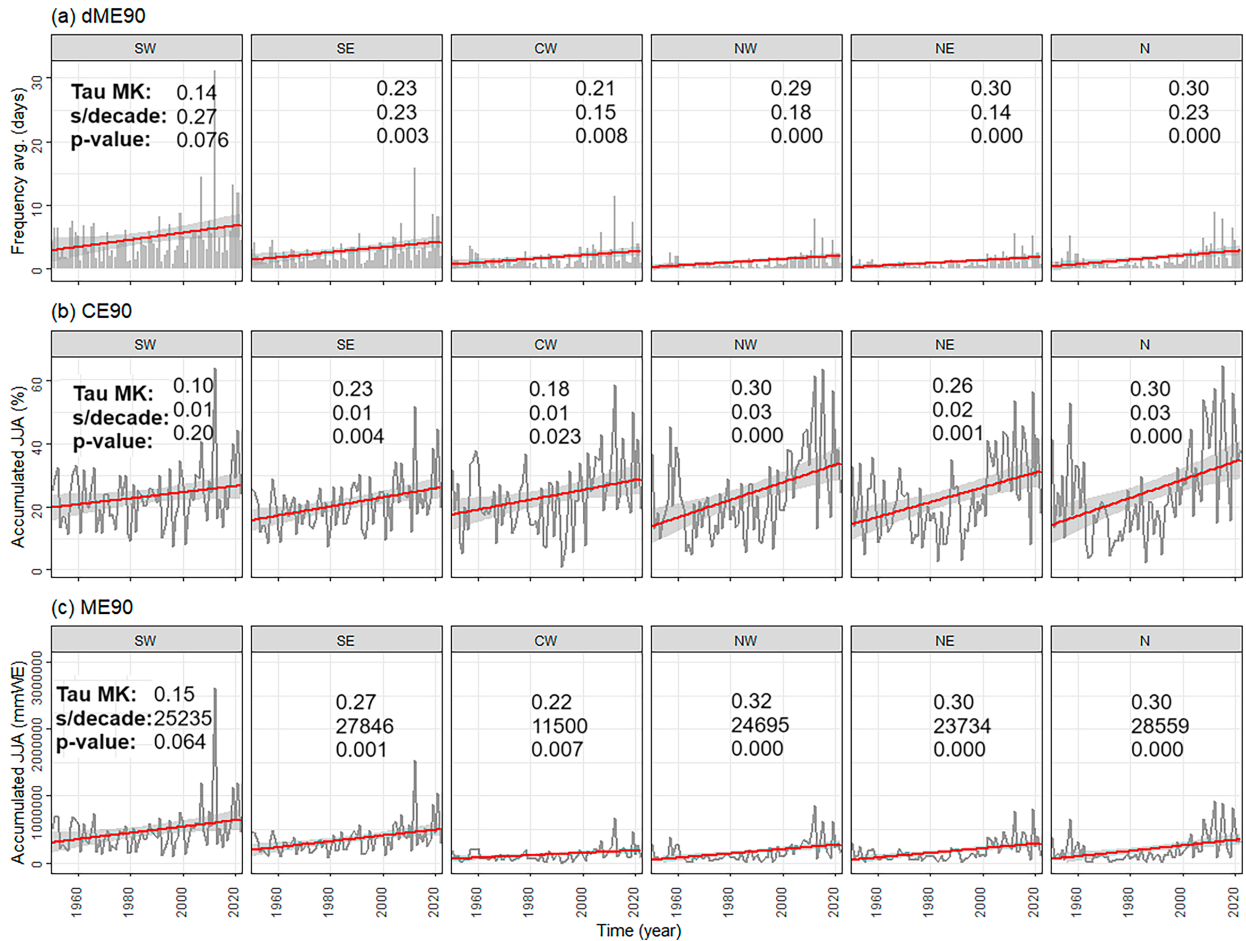


FIG. 1. (a) Total accumulated extreme (>90th percentile) melting (ME90) for each sector and year during summer. (b) Average percentage of the total accumulated extreme melting over the total melting (CE90) for each sector and year during summer. (c) Average extreme melting frequency for each sector and year during summer (dME90). The solid line indicates the linear regression. The shaded area indicates the confidence interval at 95%. The ME and dME time series for average melting days; 97th and 99th percentile ranks can be consulted in the supplemental material (Figs. S2–S4).

longer than 20 years (Fig. 3). The largest and statistically significant increases were detected in the near coastal areas, consistent with trends in extreme melting intensity. Notably, dME90 exhibited a marked increase in accumulation sectors during the 1990–2022 period (Fig. 2). Long-term dME90 trends were mostly statistically significant, with the highest increments detected across the NE (tau MK = 0.30; p value < 0.01) and N (tau MK = 0.30; p value < 0.01) sectors. In contrast, the SW and central-western (CW) sectors showed the lowest dME90 trends (tau MK = 0.14 and 0.21, respectively). A comparison between dME90 and dME trends revealed similar spatial patterns (Fig. 2), but higher magnitude trends for the latter indicator (Fig. 1 and Fig. S1). For dME, the largest increases in tau MK were found in N and NW, while lower rates were detected in SW and CW (Fig. 3).

c. Surface energy balance partitioning

The SEB partitioning during extreme melting events is shown in Fig. 4. The results indicate that the energy available

for extreme melting primarily comes from SWnet, constituting the entire energy available for extreme melting in the N and NE regions (Fig. 5). Positive heat fluxes are offset by negative LWnet, particularly in the N and NE sectors where the largest LWnet during extreme events is simulated. LWnet comes from LWD rather than LWU since the snow surface temperature during melting events is limited to 0°C. Turbulent heat fluxes exhibit a low contribution to the energy available for melting during extreme episodes (Fig. 5). The second most relevant positive heat flux during extreme melting days is SHF. The contribution of SHF to the energy available for extreme melting across the GrIS ranges from 25% (SE) to 20% (NW) (Figs. 4 and 5). Turbulent heat fluxes increase toward the lower-elevation zones of GrIS, where SHF accounts for approximately 40% of the SEB (Fig. 5a). Finally, LHF has the lowest SEB contribution to extreme melting, accounting for about 1% of the SEB across all sectors. The SEB trends are presented in Figs. 5b and 5c. More energy available for melting is received due to increases in SWnet and SHF

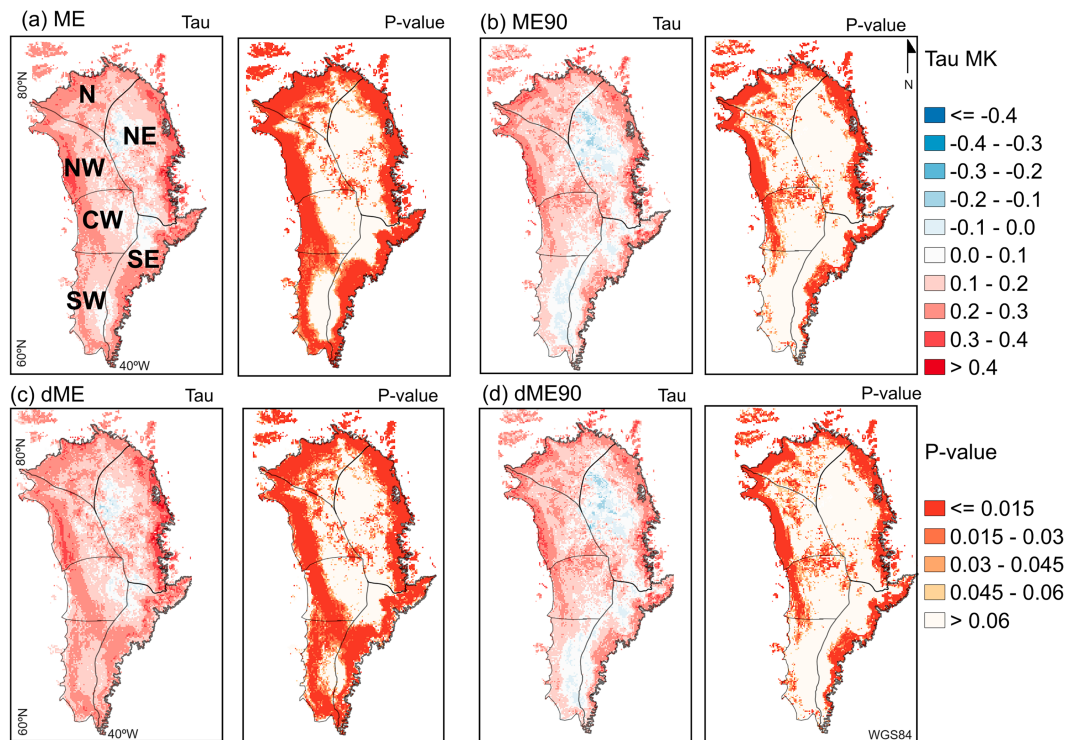


FIG. 2. Trend analysis across the GrIS (1950–2022). Maps show the tau MK and p values from the tau MK analysis for (a) accumulated summer melting (ME); (b) accumulated summer extreme melting (>90th percentile) per season (ME90); (c) number of melting days per season (dME); and (d) number of summer extreme melting days per season (dME90).

(tau MK ≥ 0.15), which exhibit similar spatial trend distributions across most of the GrIS. LWnet shows the largest downward trend during melting days (tau MK ≥ 0.30). Trends are statistically nonsignificant at the 95% level for most areas. The SEB trends shown here are consistent with warming across the entire ice sheet (Fig. S5).

d. Atmospheric circulation patterns

The atmospheric circulation in Greenland during summer is clustered into 20 CWTs (Fig. 6). Substantial differences in melting and SEB are found during similar synoptic configurations due to the origin of air masses, flow direction, and topographical barrier effects imposed by the relief configuration.

The relative frequency of CWTs is presented in Fig. S6. Most of the days in June are categorized as CWT 2, accounting for 11% of the total days. In July, CWT 18 and CWT 19 are dominant, each representing 9% of the total days. In August, CWT 6 prevails, comprising 8% of the total days. CWT 1–CWT 13 are characterized by lower-than-average Z500 across the GrIS and have a low contribution to extreme melting events. CWT 1–CWT 5 rarely cause extreme melting across the GrIS (<5% dME90) (Figs. 7–9). Specifically, CWT 1 is characterized by a cyclone near the Denmark Strait, which leads to wet eastern flow and the lowest extreme melting rates across all GrIS sectors. CWT 2 presents a low barometric gradient over the GrIS, while CWT 3 brings precipitation instead of melting. The northward migration of CWT 3 results in CWT 6

and can bring some melting across the southern areas of the GrIS. CWT 4 represents a cyclonic system over the SW GrIS. Similarly, CWT 5 is characterized by a low pressure system located near the NW GrIS, leading to westerly flow over the northern GrIS and lower-than-average energy available for melting (Figs. S7–S11).

CWT 3, CWT 6, CWT 11, and CWT 12 are linked with low pressure systems in (CWT 3), above (CWT 6), and near (CWT 11 and CWT 12) the Baffin Bay. During CWT 11 and CWT 12, however, the westerly flow brings moisture to western Greenland, and foehn effects prevail across the eastern area. The cloudless conditions (Figs. S12 and S13) enhance solar radiation there (Fig. S7), leading to extreme melting episodes in NE (CWT 11) and over summit zones (CWT 12) (Fig. 7). CWT 8 and CWT 9 are characterized by the lack of clearly defined centers of action, leading to lower-than-average SEB and melting. Only during CWT 8 is extreme melting slightly higher in N (dME90 = 6% for both sectors) due to cloud radiative effects (Figs. S12 and S13). Finally, CWT 10 represents a low pressure system displaced toward the northernmost GrIS with a zonal flow and a low barometric gradient across the central and southern GrIS.

CWT 14–CWT 20 bring positive Z500 anomalies and are key synoptic configurations in extreme melting events. CWT 15–CWT 19 control extreme melting across the northern GrIS, while CWT 14, CWT 16, and CWT 20 are responsible for extreme events across the southern GrIS. The southern position of the

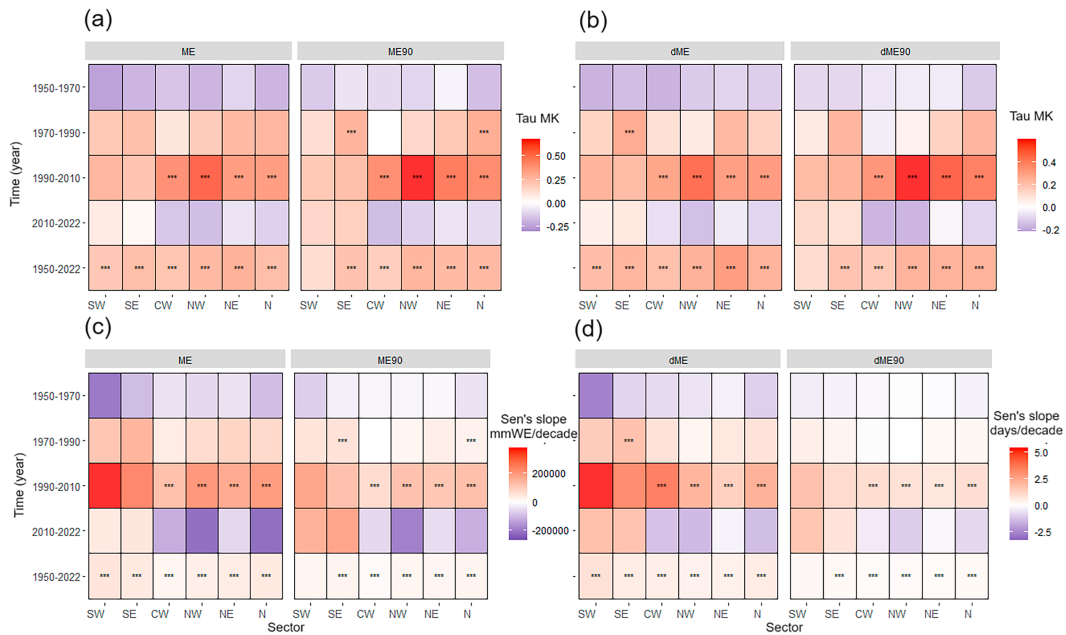


FIG. 3. Trend analysis by temporal period (y axis) and GrIS sector (x axis). (upper) The tau MK values for (a) intensity (ME and ME90) and (b) frequency (dME and dME90) indicators. (bottom) Sen's slope values for (c) intensity (ME and ME90) and (d) frequency (dME and dME90) indicators. Black asterisks inside the boxes indicate a p value lower than 0.05.

anticyclone center of action determines the spatial distribution of extreme melting and SEB partitioning. During CWT 14, a high pressure system is over the Labrador Sea. Cloudy conditions prevail across most GrIS (Figs. S12 and S13), which leads to positive LWD anomalies and dME90 events concentrated in SW (11%) and CW (6%). Meanwhile, the eastern area is exposed to high solar radiation and sensible heat fluxes, leading to dME90 events across the SE (8%). CWT 15 features an anticyclonic system over the Baffin Bay, producing stable conditions across the western and central GrIS. However, upslope winds create cloudy conditions (Figs. S12 and S13) and positive LWD

anomalies in NE and N (Fig. S9), while SWD drives dME90 events in NW (13%). CWT 16 is an omega-blocking pattern that brings extremely warm and moist subtropical air masses toward GrIS. Positive SWnet and SWD heat fluxes prevail over most of the ice sheet and SHF in the ice sheet margins. Nevertheless, higher-than-average cloud-cover conditions in the northern sectors lead to intense LWD heat fluxes there. CWT 16 is associated with the majority of ME90 across the NW sector (Fig. 8), presents the highest air temperature in GrIS of the CWT catalog (Fig. S14), and is responsible for the most extreme melting episodes in GrIS. CWT 17 features a high pressure

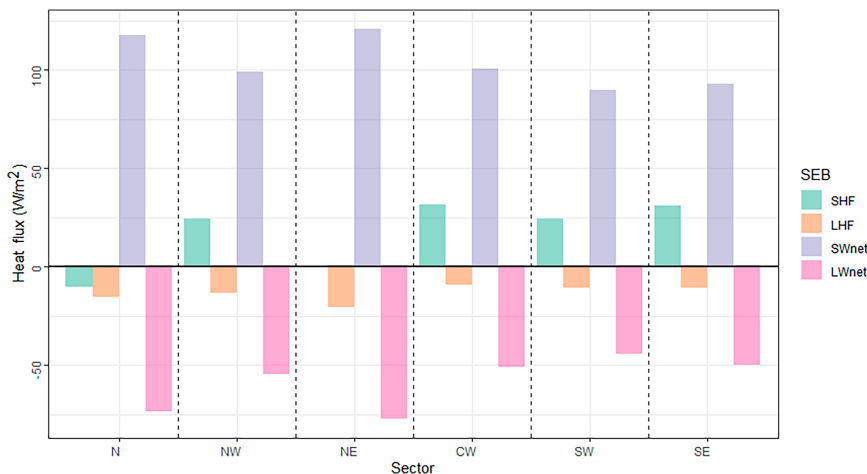


FIG. 4. Average SEB per sector during extreme melting events.

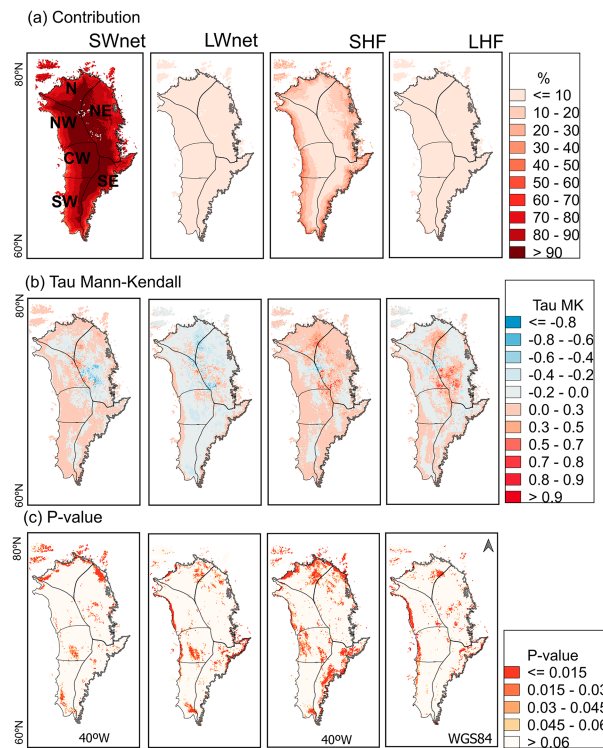


FIG. 5. (a) SEB component contribution (%) to the energy available for melting during extreme melting events. The SEB contribution to extreme melting is calculated by summing the positive energy from the SEB components during extreme melting events, dividing this sum by the total positive energy, and multiplying by 100. Spatial trend analysis of SEB, including (b) tau MK and (c) p values during melting days.

system in the Greenland Sea and a low-pressure area in southern-eastern Greenland, leading to positive SWnet and SWD heat fluxes across the northern and western GrIS. CWT 17 is responsible for dME90 events in NE and N (10% and 12%, respectively). CWT 18 is distinguished by a high pressure system over the central Arctic Ocean, which leads to stable weather conditions and cloud-free conditions over most GrIS, leading to melting due to enhanced shortwave radiation. On the contrary, cloud cover increases LWD in northern GrIS and results in large dME90 days (23%). CWT 19 involves a high pressure center of action near Iceland and southerly flow, leading to dME90 over SE (11%) and NE (10%). High-cloud cover prevails in NW, CW, SW, and SE GrIS (Figs. S12 and S13), which enhance melting due to positive LWD anomalies (Fig. S9), whereas in NE GrIS, positive SWD, SWnet, and SHF heat fluxes control melting (Figs. S7–S10). CWT 13 presents a similar configuration to CWT 20. However, the high pressure system is displaced toward the south for CWT 13, resulting in a low contribution to extreme melting. CWT 20 presents a high pressure center over the SE GrIS strip, with the south-westerly warm and moist flow, resulting in a contrasted west-east (W–E) SEB pattern like CWT 14. Melting is controlled by longwave radiation and turbulent heat fluxes across the

western area, while topographical barrier effects reduce cloud cover (Figs. S12 and S13) across the eastern GrIS, where shortwave radiation drives melting. CWT 20 rules most ME90 and dME90 events in SW (21%), CW (14%), and SE (14% days).

The occurrence and intensity of extreme melting events in GrIS are greatly influenced by anticyclonic weather types from CWT 14 to CWT 20, which exhibit a nonstatistically significant upward trend. On the other hand, cyclonic types show a downward trend. Small differences were observed between the 1950–2022 and 1990–2022 periods for most synoptic configurations (Fig. 10). Among the CWTs, CWT 16, which is associated with the most extreme melting events across the NW (Fig. 9), has exhibited the largest increase (p value = 0.06; Fig. 10). CWT 20, which results in the most extreme melting events across the SW and SE, shows an increase for the recent 1990–2022 period (Fig. 10). Moreover, CWT 8 and CWT 18, which are characterized by low barometric gradient over GrIS and melting across the northern GrIS, have also shown an upward trend, although this trend is not statistically significant. In contrast, CWT 1–CWT 13, which mostly do not lead to extreme melting events, have shown a negative trend, with statistically significant trends observed only for CWT 1 and CWT 13. The remaining CWTs have displayed small, nonstatistically significant changes (Fig. 10 and Fig. S15).

4. Discussion

a. Extreme melting trends and its related impacts

The spatiotemporal evolution of extreme summer melting in GrIS reveals robust increases across all percentile ranks analyzed, including the 90th, 97th, and 99th percentiles. ME90 increased across most of the northern GrIS, and long-term trends from 1950 to 2022 are statistically significant at the 99% level over most lower-elevation areas. These areas are closer to the 0°C isothermal conditions in average during the entire summer and exposed to higher energy available for melting during extreme events as well as atmospheric flow originating from ocean areas. Similarly, ME90 and dME90 showed an upward trend across GrIS, with the largest values detected across the NW and NE sectors. These trends are consistent with previous studies that suggest that extreme melting episodes in recent decades have been rarely observed in paleoclimate records, and only a similar extreme melting event to that in 2012 was previously detected in 1889 and around once every 250 years between 1000 and 4000 cal year BP according to paleoclimate reconstructions based on ice core proxies (Alley and Anandkrishnan 1995; Nghiem et al. 2012). The reported melting trends are in accordance with air temperature evolution for the same temporal period (Fig. S5) and are consistent with long-term warming and SMB evolution (Fettweis et al. 2017). Extreme melting trends in NW are consistent with the statistically significant upward trend in summer ice-surface temperatures (ca. 1.35°C, $\pm 0.47^\circ\text{C decade}^{-1}$) reported for the NW edge of GrIS from 2002 to 2012 (Hall et al. 2013). Melting has also enhanced the upward displacement of the equilibrium line altitude (ELA) by 44 m a⁻¹

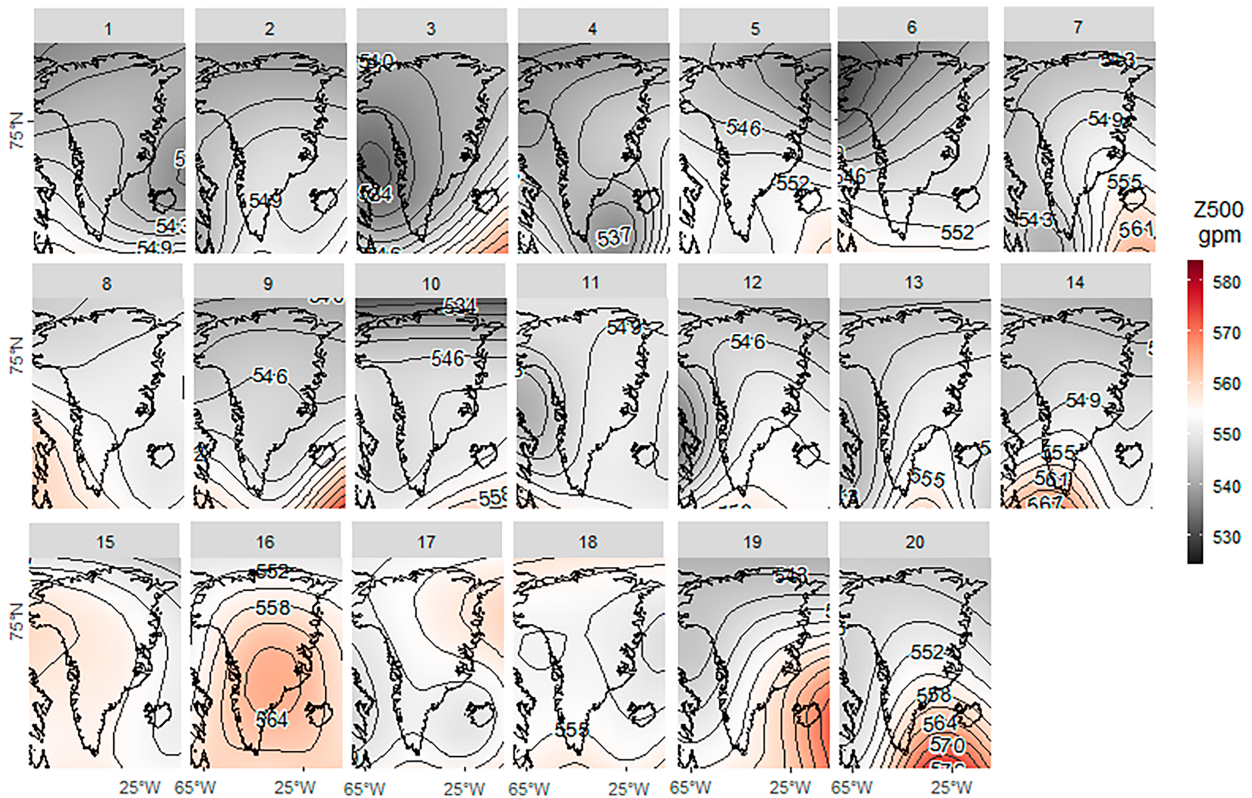


FIG. 6. Spatial representation of the synoptic configurations prevailing in Greenland during summer. The colors show the average Z500 (gpm) for each CWT.

from 1996 to 2011 in West GrIS (McGrath et al. 2013), contributing to the expansion of the ablation zone and the upward migration of the dry snow zones across the GrIS (Noël et al. 2019).

CE90 evolution shows a statistically significant upward trend for all sectors. CE90 typically contributes to 40% of the melting of GrIS, but only four days of extreme melting in July 2012 contributed to 20% of the total accumulated summer melting (Fausto et al. 2016). Except in NW, NE, and N, the reported increase in extreme melting is slightly lower than the ME and dME trends suggesting that the total accumulated summer melting is equally driven by average (nonextreme) melting days. Higher-than-average melting seasons, rather than extreme events, can enhance extreme melting events in subsequent years since extreme episodes are preconditioned by climate and melting anomalies from previous years. For instance, the extreme melting event of 2012 was amplified by unprecedented anticyclonic conditions from 2007 to 2010, which were the most intense since the NCEP–NCAR records (1948) (Hanna et al. 2012).

The depletion of snow over the ice sheet also causes surface darkening and accelerates melting in the following days (Box et al. 2012). Positive melt anomalies in previous years (e.g., 2002, 2005, 2007, 2010, and 2011) reduce the albedo to low levels, leading to bare ice exposure (Tedesco and Fettweis 2020). The exceptional warm conditions during extreme events facilitate the migration of the snow line to higher

elevations (Ryan et al. 2019). Melting events can cause water infiltration and snowpack refreezing over the ice layer (Harper et al. 2012). However, during extreme melt events, such as in July 2012, the infiltration capacity was exceeded for some GrIS sectors, such as in Kangerlussuaq (western GrIS), which led to an extreme proglacial discharge event amplified by the ice sheet hypsometry (Mikkelsen et al. 2016). Melting events can result in the expansion of the melt area, leading to faster thinning and steepening of the ice sheet (Colgan et al. 2011). This can trigger the expansion of crevasses and moulins (Chandler and Hubbard 2023), causing the transport of meltwater by the englacial and subglacial systems (Poinar et al. 2015). These extreme events can also bring about structural changes in the ice sheet by creating surface melt layers that increase water infiltration in subsequent years (Culberg et al. 2021). The formation of new moulins and crevasses across the accumulation zone (Colgan et al. 2011), in combination with the development of supraglacial lakes (e.g., Howat et al. 2013; How et al. 2021), snow grain growth, and deposition of light-absorbing impurities (Dumont et al. 2014), can further amplify albedo decay and melting (Williamson et al. 2020).

b. Thermodynamic drivers of extreme melting

Warming and moisture advection play a relevant role in extreme melting events by increasing sensible and enhancing cloud radiative effects through longwave radiative fluxes, as shown in Figs. S9–S11. During anticyclonic weather types,

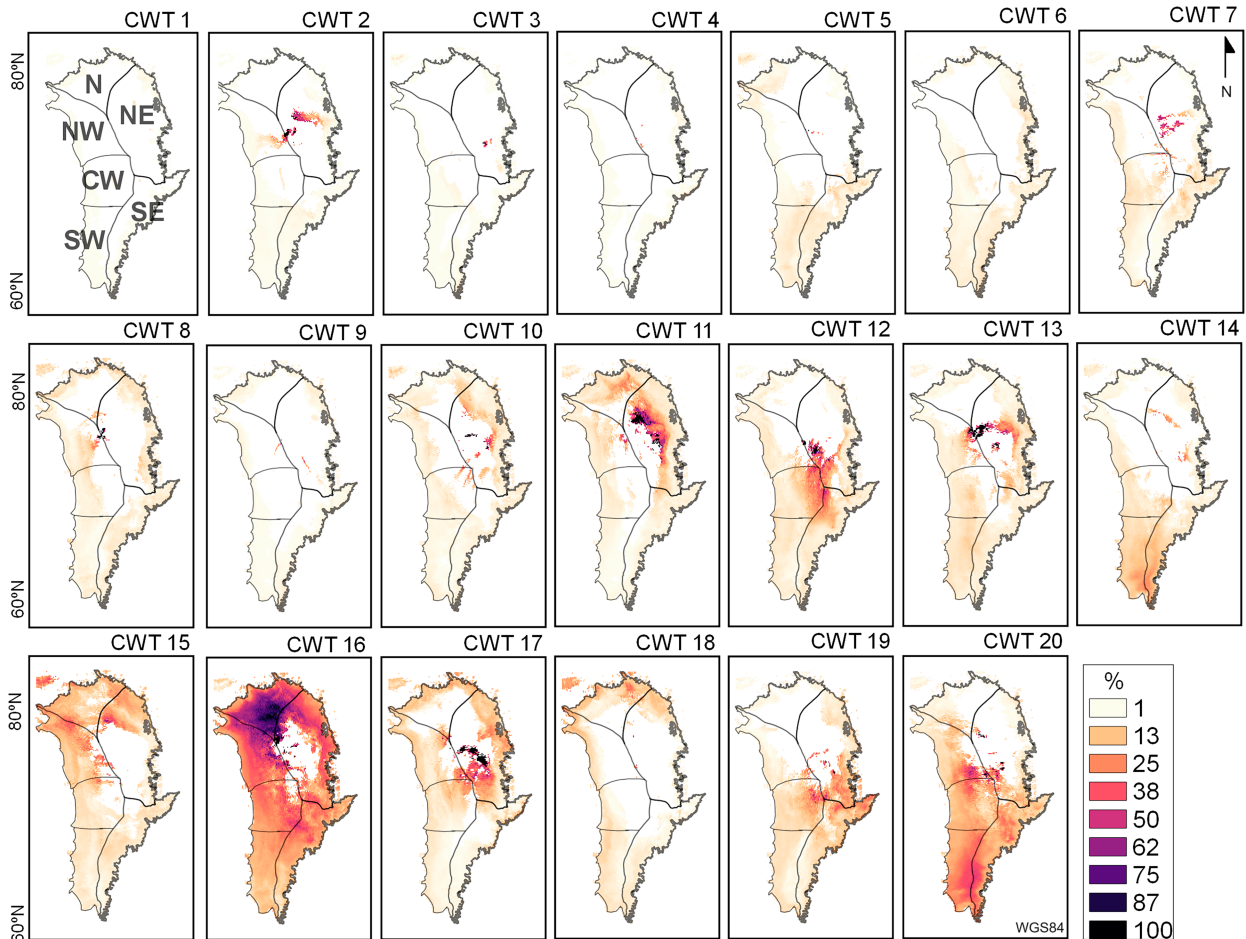


FIG. 7. Percentage of contribution of the accumulated ME90 during each CWT to the total accumulated ME90.

extreme melting across the northern area is often associated with positive downward longwave heat flux anomalies. This sector shows higher-than-average cloud cover, which forms along the coastline due to upslope winds and condensation, as examined in previous studies (Hahn et al. 2018; Delhasse et al. 2018; Mattingly et al. 2018; Ward et al. 2020). CWT 16, which controls ME90 across the NW through positive downward longwave heat flux anomalies, exhibits the largest upward trend in frequency for the 1950–2022 period and explains the highest extreme melting trends detected in this sector. These findings are consistent with previous studies that reported thin low-level liquid clouds during the 2012 extreme melting episode, allowing downwelling shortwave radiation fluxes to warm the near-surface region while preventing escaping downward infrared fluxes (Bennartz et al. 2013). The increase in extreme melting (Figs. 2 and 3) is in line with the observed increase in runoff since the 1990s in northern GrIS; these higher-than-average trends have been attributed to a decrease in albedo and an increase in cloud cover, leading to positive net radiation anomalies (Van Tricht et al. 2016; Cullather and Nowicki 2018; Välisuo et al. 2018; Noël et al. 2019) and warming trends (1982–2011; $2.7^{\circ} \pm 0.33^{\circ}\text{C}$) in North Greenland

(Orsi et al. 2017). While summer cloud cover has increased in northern GrIS during recent decades, the opposite trend has been observed in southern GrIS, leading to faster albedo decay and increased SWnet (Lim et al. 2016; Hofer et al. 2017; Niwano et al. 2019).

The contribution of absorbed shortwave radiation to the surface energy balance during extreme events across the SW and CW zones is lower than average due to their exposure to warm, wet westerlies and subtropical southwesterly flow that enhances cloudy conditions, reduces SWD, and increases turbulent heat fluxes and emissivity. These findings are consistent with previous characterizations of the western SEB ablation areas (Ward et al. 2020; Box et al. 2023) and observations during the extreme melting episode of July 2012, when nonradiative heat fluxes accounted for one-third of the SEB partitioning across the ablation zone of the southern–western Greenland (Fausto et al. 2016).

Across the southern and central–eastern sectors of the GrIS, the extreme melting is primarily caused by shortwave radiation driven by CWT 14, CWT 15, CWT 16, CWT 18, and CWT 20 episodes, as the topographical barriers reduce westerly exposure. Moreover, strong foehn effects prevail across

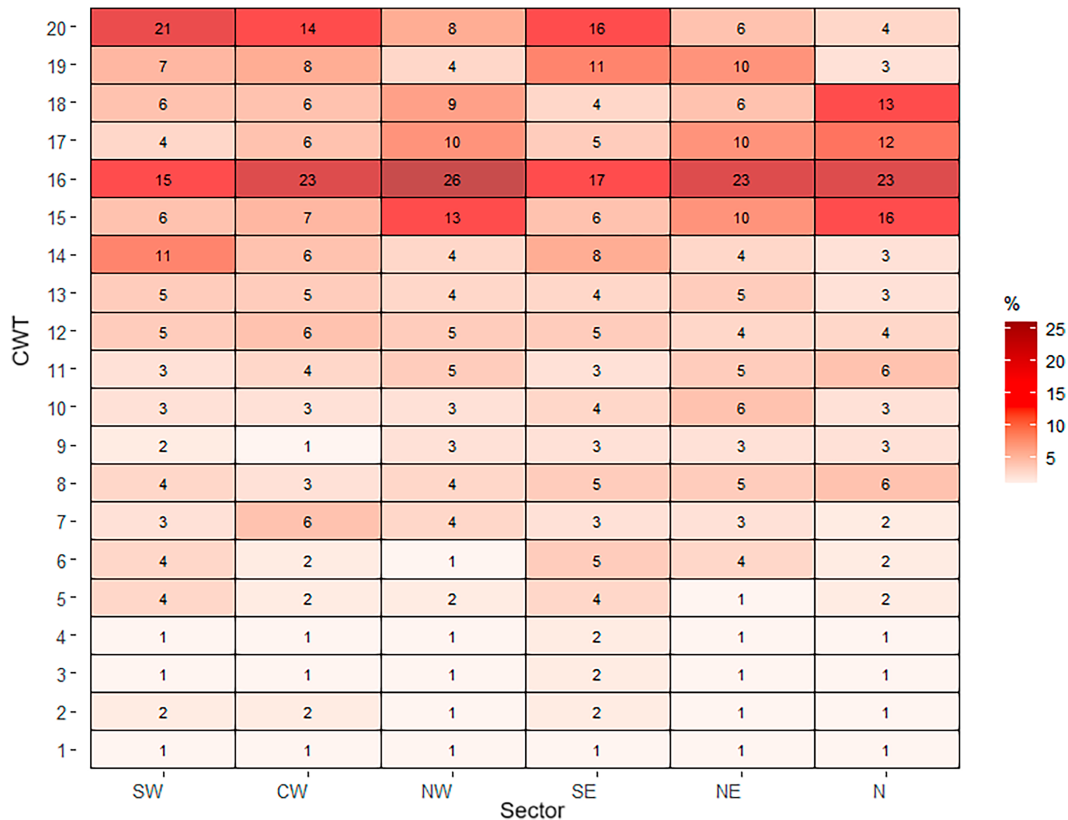


FIG. 8. Frequency of dME90 days grouped by GrIS sector (x axis) and CWT (y axis).

the eastern GrIS, caused by Baffin Bay cyclonic weather types (CWT 11 and CWT 12). Previous studies have also linked melting in this sector to onshore winds that flow downslope the GrIS coastline (Mote 1998; Fettweis et al. 2011; Noël et al. 2019; McLeod and Mote 2016; Cullather and Nowicki 2018; Välisuo et al. 2018; Mattingly et al. 2020; Preece et al. 2023; Mattingly et al. 2023). The eastern katabatic winds are strong enough to reduce the local ocean airflow advection (Mioduszewski et al. 2016), and large yearly positive melting anomalies have been previously detected in coastal areas due to subsidence heating and zonal winds (Välisuo et al. 2018).

c. Large-scale circulation

The results of this study indicate that specific anticyclonic weather types are responsible for driving extreme melting events (Fig. 9). The increase in extreme melting observed in our work is attributed to the upward (downward) frequency trends of anticyclonic (cyclonic) weather types (Fig. 10) combined with an increase in energy available for melting (Fig. 5b). The center and flow of high pressure systems are crucial in determining the GrIS sector where extreme melting occurs. In northern GrIS, extreme melting is driven by the increase in CWT from 15 to 18. The highest frequency and intensity of extreme melting detected across the NW is mostly due to the higher frequency of CWT 16. Variability in southern extreme melting is primarily controlled by CWT 14, CWT 16, and CWT 20. Thus, the ME90 trends across the SW and SE sectors are influenced by

the small change observed for CWT 20 during the period from 1950 to 2022.

The results indicate that the observed increase in extreme melting over GrIS can be attributed to the increase in anticyclonic weather types (Fig. 10) which is linked with the negative summer NAO, positive GBI, and AMO trends (Hanna et al. 2012; McLeod and Mote 2016) and the increase in energy available for melting during extreme melting episodes (Figs. 4b,c). The long-term increase in meltwater and runoff over GrIS is consistent with these factors and is mostly (70%) explained by the increase in high pressure systems from 1993 to 2012 (Fettweis et al. 2013). Other works also suggest that atmospheric circulation variability is responsible for a considerable (40%) proportion of GrIS melting from 1948 to 2013 (Rajewicz and Marshall 2014). Välisuo et al. (2018) analyzed melting episodes during summer in GrIS for the 2000–14 period and found that differences between high (e.g., 2012) and low (e.g., 2013) melting years have been explained by the higher frequency of southern airmass advection. Häkkinen et al. (2014) reported that the frequent occurrence of blocking and warm subtropical airmass advections led to most of the melting for the 2000–12 period. These findings are consistent with the statistically significant increase in the omega-blocking pattern (CWT 16) and the long-term frequency of blocking over GrIS (Hanna et al. 2013; Preece et al. 2023).

It is expected that the frequency and intensity of GrIS melting will continue to increase in the future (IPCC 2022), and

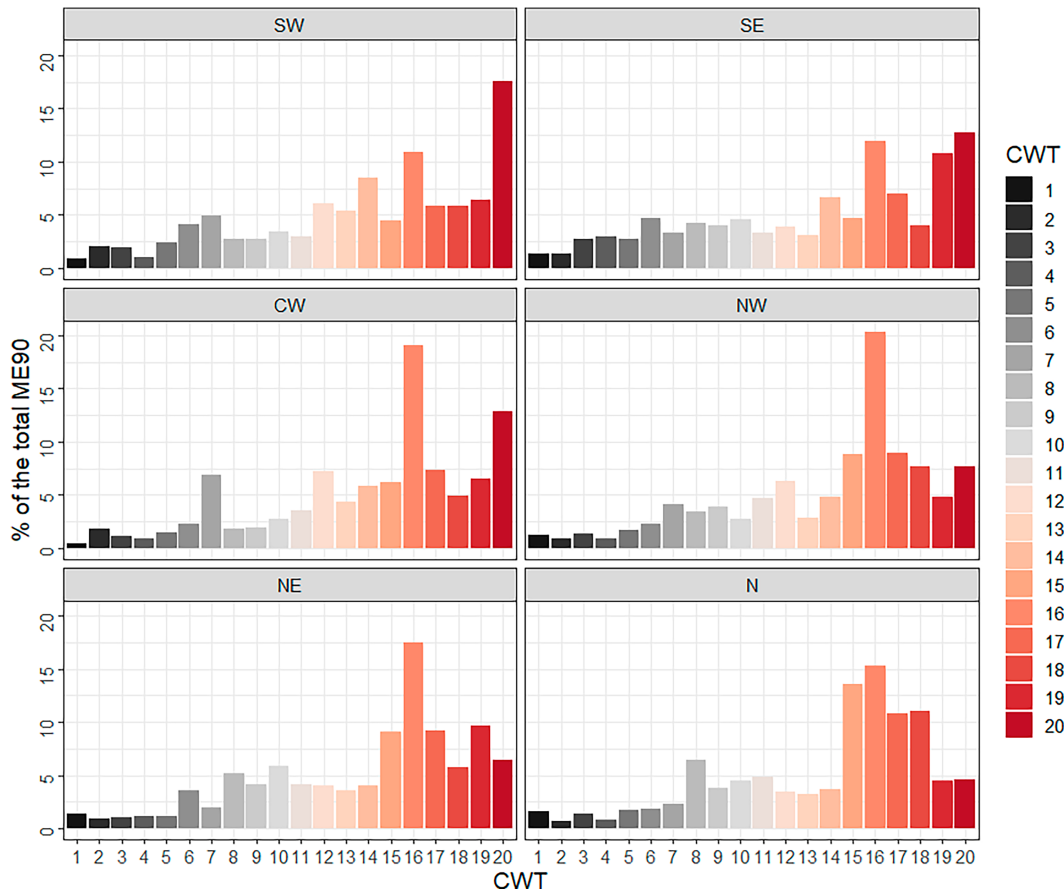


FIG. 9. Contribution of each CWT to the total accumulated ME90 by GrIS sector.

the upward trends in extreme melting reported in this study are likely to continue. While this study focused on the recent past, future research should examine the evolution of extreme melting frequency and intensity. Climate projections indicate snowfall increases at high latitudes, including GrIS (Räsänen 2008; Brutel-Vuilmet et al. 2013; Bintanja and Andry 2017; Krasting et al. 2013), but even the relatively small increases in precipitation toward the end of the midcentury (2100) and under high-emission scenarios (RCP8.5) will not be sufficient to counterbalance the anticipated large increase in surface summer meltwater and runoff (Vizcaino et al. 2014). Future CMIP6 projections suggest that GrIS meltwater will be even larger than previous CMIP5 projections due to feedback strengths of clouds and sea ice cover (Hofer et al. 2017), potentially leading to more extreme melting events across GrIS.

5. Conclusions

The GrIS meltwater and its associated runoff substantially contribute to global sea level rise. With climate heating underway, it is imperative to enhance our comprehension of extreme GrIS melting events and their atmospheric drivers. Here, we evaluated the frequency and intensity of extreme

GrIS melting trends in GrIS (1950–2022) and its surface energy balance and atmospheric circulation drivers.

Our findings suggest that extreme melting events have demonstrated a general positive trend across most GrIS sectors, indicators, and percentile ranks considered. However, the trend in extreme melting events is slightly lower than that of the average melting trend. Statistically significant trends were most evident across the coastline areas due to the proximity of 0°C isothermal conditions and warm and humid oceanic airflows. CE90 exhibited a statistically significant upward trend at a 99% confidence level for all sectors. Consistent with previous studies, the highest trends were detected across the northern GrIS, specifically NW.

The evolution of extreme melting is largely influenced by large-scale circulation variability. The location of the anticyclone center of action and flow determines the GrIS sector in which extreme melting events occur. As we analyze higher percentile ranks, the contribution of blocking events to melting increases. The upward frequency of anticyclonic weather types during the analyzed period, combined with the increase in energy available for melting during extreme melting episodes, explains the rise in extreme melting events detected in most GrIS sectors. The greatest trends in extreme melting are observed across the northern GrIS, mainly due to the upward

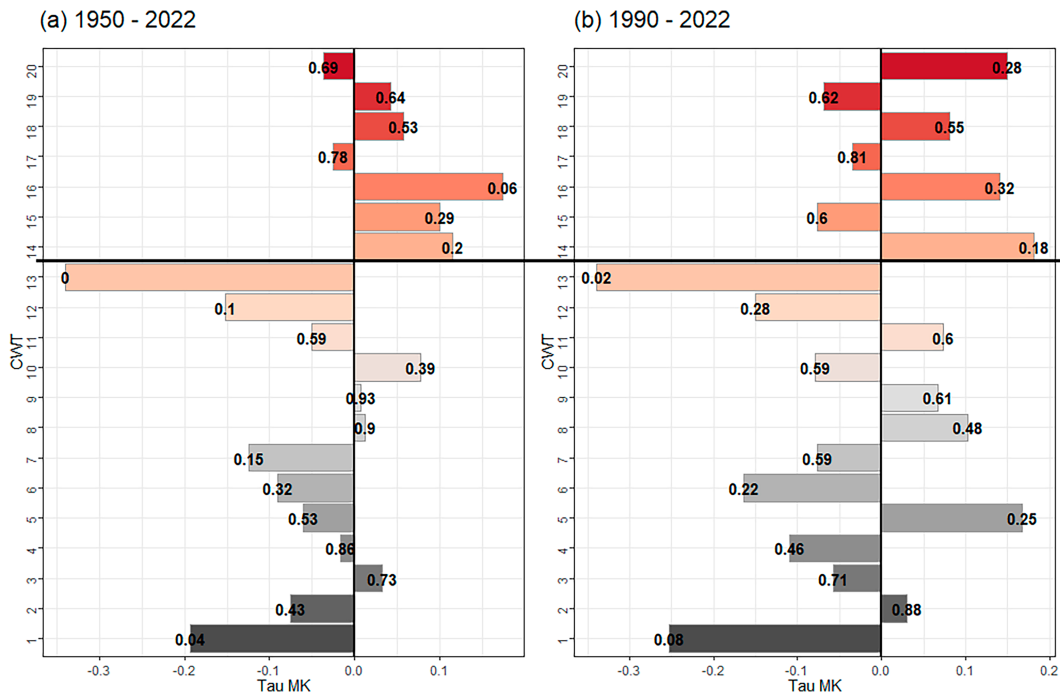


FIG. 10. CWT trend analysis (tau MK values) for the (a) 1950–2022 and (b) 1990–2022 periods. The black letters indicate the p value. The CWTs that lead to dME90 episodes (CWT 14 to CWT 20; Figure) are shown over the horizontal black line.

frequency trends of CWT 15–CWT 19, which controls extreme melting in this sector. An omega-blocking pattern (CWT 16) leads to large radiation anomalies in most of the GrIS and extreme melting across the NW, explaining the highest trends simulated for this sector. Across the southern and central regions of GrIS, the intensity and frequency of extreme melting are influenced by CWT 20, causing large positive anomalies in SHF and LWD across the western GrIS and SWD across the eastern GrIS. The smaller trends reported in these sectors can be explained by the small trends observed for CWT 20 from 1950 to 2022. However, the higher frequency in CWT 20 since the 1990s likely explains the higher-than-average extreme melting trend observed in these sectors during recent decades.

This study has provided insights into the spatiotemporal evolution of extreme melting events across the GrIS and the climate drivers that influence them. The results are consistent with previous research and confirm the negative NAO and positive GBI evolution during the summer period analyzed. Future research should investigate the impact of these long-term extreme melting trends on the GrIS ecosystem and assess whether similar trends will persist in the future.

Acknowledgments. The work was supported by the NEOGREEN project of “Antarctic, Arctic, Alpine Environments-ANTALP” and MARGISNOW (PID2021-124220OB-I00), both funded by the Spanish Ministry of Science, Innovation and Universities. ANTALP research group is also funded by the Government of Catalonia

(2017-SGR-1102). J. B. is supported by a predoctoral University FPI Grant (PRE2021-097046) funded by the Spanish Ministry of Science, Innovation and Universities. The authors are grateful to Dr. Shawn Marshall, the editor, and two anonymous reviewers for their valuable feedback. Conceptualization: J. B., M. O., J. I. L. M., and X. F. Data provision: X. F. Data analysis: J. B. Writing—original draft: J. B. Writing—review and editing: J. B., M. O., J. I. L. M., and X. F. Funding acquisition: J. I. L. M., and M. O.

Data availability statement. The MAR code is available at <https://www.mar.cnrs.fr>, and the MAR output is available at <ftp://ftp.climato.be/fettweis> (last access: 11 May 2023). NCEP–NCAR reanalysis data are available at <https://psl.noaa.gov/data/gridded/data.ncep.reanalysis.html> (last access: 11 May 2023), and ERA5 data are available at <https://cds.climate.copernicus.eu/> (last access: 11 May 2023).

REFERENCES

- Alley, R. B., and S. Anandakrishnan, 1995: Variations in melt-layer frequency in the GISP2 ice core: Implications for Holocene summer temperatures in central Greenland. *Ann. Glaciol.*, **21**, 64–70, <https://doi.org/10.3189/S026030500015615>.
- Antwerpen, R. M., M. Tedesco, X. Fettweis, P. Alexander, and W. J. Van de Berg, 2022: Assessing bare-ice albedo simulated by MAR over the Greenland Ice Sheet (2000–2021) and implications for meltwater production estimates. *Cryosphere*, **16**, 4185–4199, <https://doi.org/10.5194/tc-16-4185-2022>.

- Bennartz, R., and Coauthors, 2013: July 2012 Greenland melt extent enhanced by low-level liquid clouds. *Nature*, **496**, 83–86, <https://doi.org/10.1038/nature12002>.
- Bintanja, R., and O. Andry, 2017: Towards a rain-dominated Arctic. *Nat. Climate Change*, **7**, 263–267, <https://doi.org/10.1038/nclimate3240>.
- Bonsoms, J., S. Gonzalez, M. Prohom, P. Esteban, F. Salvador-Franch, J. I. López-Moreno, and M. Oliva, 2021: Spatio-temporal patterns of snow in the Catalan Pyrenees (NE Iberia). *Int. J. Climatol.*, **41**, 5676–5697, <https://doi.org/10.1002/joc.7147>.
- , J. I. López-Moreno, S. González, and M. Oliva, 2022: Increase of the energy available for snow ablation in the Pyrenees (1959–2020) and its relation to atmospheric circulation. *Atmos. Res.*, **275**, 106228, <https://doi.org/10.1016/j.atmosres.2022.106228>.
- Box, J. E., 2013: Greenland Ice Sheet mass balance reconstruction. Part II: Surface mass balance (1840–2010). *J. Climate*, **26**, 6974–6989, <https://doi.org/10.1175/JCLI-D-12-00518.1>.
- , X. Fettweis, J. C. Stroeve, M. Tedesco, D. K. Hall, and K. Steffen, 2012: Greenland Ice Sheet albedo feedback: Thermodynamics and atmospheric drivers. *Cryosphere*, **6**, 821–839, <https://doi.org/10.5194/tc-6-821-2012>.
- , and Coauthors, 2022: Greenland Ice Sheet climate disequilibrium and committed sea-level rise. *Nat. Climate Change*, **12**, 808–813, <https://doi.org/10.1038/s41558-022-01441-2>.
- , and Coauthors, 2023: Greenland Ice Sheet rainfall climatology, extremes and atmospheric river rapids. *Meteor. Appl.*, **30**, e2134, <https://doi.org/10.1002/met.2134>.
- Brun, E., P. David, M. Sudul, and G. Brunot, 1992: A numerical model to simulate snow-cover stratigraphy for operational avalanche forecasting. *J. Glaciol.*, **38**, 13–22, <https://doi.org/10.3189/S0022143000009552>.
- Brutel-Vuilmet, C., M. Ménégoz, and G. Krinner, 2013: An analysis of present and future seasonal Northern Hemisphere land snow cover simulated by CMIP5 coupled climate models. *Cryosphere*, **7**, 67–80, <https://doi.org/10.5194/tc-7-67-2013>.
- Chandler, D. M., and A. Hubbard, 2023: Widespread partial-depth hydrofractures in ice sheets driven by supraglacial streams. *Nat. Geosci.*, **16**, 605–611, <https://doi.org/10.1038/s41561-023-01208-0>.
- Colgan, W., K. Steffen, W. S. McLamb, W. Abdalati, H. Rajaram, R. Motyka, T. Phillips, and R. Anderson, 2011: An increase in crevasse extent, West Greenland: Hydrologic implications. *Geophys. Res. Lett.*, **38**, L18502, <https://doi.org/10.1029/2011GL048491>.
- Constable, A. J., S. Harper, J. Dawson, K. Holsman, T. Mustonen, D. Piepenburg, and B. Rost, 2022: Cross-chapter paper 6: Polar regions. *Climate Change 2022: Impacts, Adaptation and Vulnerability*, Cambridge University Press, 2319–2368.
- Culberg, R., D. M. Schroeder, and W. Chu, 2021: Extreme melt season ice layers reduce firn permeability across Greenland. *Nat. Commun.*, **12**, 2336, <https://doi.org/10.1038/s41467-021-22656-5>.
- Cullather, R. I., and S. M. J. Nowicki, 2018: Greenland Ice Sheet surface melt and its relation to daily atmospheric conditions. *J. Climate*, **31**, 1897–1919, <https://doi.org/10.1175/JCLI-D-17-0447.1>.
- de La Peña, S., and Coauthors, 2015: Changes in the firn structure of the western Greenland Ice Sheet caused by recent warming. *Cryosphere*, **9**, 1203–1211, <https://doi.org/10.5194/tc-9-1203-2015>.
- Delhase, A., X. Fettweis, C. Kittel, C. Amory, and C. Agosta, 2018: Brief communication: Impact of the recent atmospheric circulation change in summer on the future surface mass balance of the Greenland Ice Sheet. *Cryosphere*, **12**, 3409–3418, <https://doi.org/10.5194/tc-12-3409-2018>.
- , C. Kittel, C. Amory, S. Hofer, D. Van As, R. S. Fausto, and X. Fettweis, 2020: Brief communication: Evaluation of the near-surface climate in ERA5 over the Greenland Ice Sheet. *Cryosphere*, **14**, 957–965, <https://doi.org/10.5194/tc-14-957-2020>.
- De Ridder, K., and H. Gallé, 1998: Land surface-induced regional climate change in southern Israel. *J. Appl. Meteor.*, **37**, 1470–1485, [https://doi.org/10.1175/1520-0450\(1998\)037%3C1470:LSIRCC%3E2.0.CO;2](https://doi.org/10.1175/1520-0450(1998)037%3C1470:LSIRCC%3E2.0.CO;2).
- Dumont, M., and Coauthors, 2014: Contribution of light-absorbing impurities in snow to Greenland's darkening since 2009. *Nat. Geosci.*, **7**, 509–512, <https://doi.org/10.1038/ngeo2180>.
- Esteban, P., P. D. Jones, J. Martín-Vide, and M. Mases, 2005: Atmospheric circulation patterns related to heavy snowfall days in Andorra, Pyrenees. *Int. J. Climatol.*, **25**, 319–329, <https://doi.org/10.1002/joc.1103>.
- Fausto, R. S., D. Van As, J. E. Box, W. Colgan, P. L. Langen, and R. H. Mottram, 2016: The implication of nonradiative energy fluxes dominating Greenland Ice Sheet exceptional ablation area surface melt in 2012. *Geophys. Res. Lett.*, **43**, 2649–2658, <https://doi.org/10.1002/2016GL067720>.
- Fettweis, X., G. Mabilbe, M. Erpicum, S. Nicolay, and M. van den Broeke, 2011a: The 1958–2009 Greenland Ice Sheet surface melt and the mid-tropospheric atmospheric circulation. *Climate Dyn.*, **36**, 139–159, <https://doi.org/10.1007/s00382-010-0772-8>.
- , M. Tedesco, M. Van den Broeke, and J. Ettema, 2011b: Melting trends over the Greenland Ice Sheet (1958–2009) from spaceborne microwave data and regional climate models. *Cryosphere*, **5**, 359–375, <https://doi.org/10.5194/tc-5-359-2011>.
- , B. Franco, M. Tedesco, J. H. Van Angelen, J. T. M. Lenaerts, M. R. Van den Broeke, and H. Gallée, 2013: Estimating the Greenland Ice Sheet surface mass balance contribution to future sea level rise using the regional atmospheric climate model MAR. *Cryosphere*, **7**, 469–489, <https://doi.org/10.5194/tc-7-469-2013>.
- , and Coauthors, 2017: Reconstructions of the 1900–2015 Greenland Ice Sheet surface mass balance using the regional climate MAR model. *Cryosphere*, **11**, 1015–1033, <https://doi.org/10.5194/tc-11-1015-2017>.
- , and Coauthors, 2020: GrSMBMIP: Intercomparison of the modelled 1980–2012 surface mass balance over the Greenland Ice Sheet. *Cryosphere*, **14**, 3935–3958, <https://doi.org/10.5194/tc-14-3935-2020>.
- Francis, J. A., and S. J. Vavrus, 2012: Evidence linking Arctic amplification to extreme weather in mid-latitudes. *Geophys. Res. Lett.*, **39**, L06801, <https://doi.org/10.1029/2012GL051000>.
- Franco, B., X. Fettweis, and M. Erpicum, 2013: Future projections of the Greenland Ice Sheet energy balance driving the surface melt. *Cryosphere*, **7** (1), 1–18, <https://doi.org/10.5194/tc-7-1-2013>.
- Gallagher, M. R., H. Chepfer, M. D. Shupe, and R. Guzman, 2020: Warm temperature extremes across Greenland connected to clouds. *Geophys. Res. Lett.*, **47**, e2019GL086059, <https://doi.org/10.1029/2019GL086059>.
- Gallée, H., and G. Schayes, 1994: Development of a three-dimensional meso- γ primitive equations model: Katabatic winds simulation in

- the area of Terra Nova Bay, Antarctica. *Mon. Wea. Rev.*, **122**, 671–685, [https://doi.org/10.1175/1520-0493\(1994\)122<0671:DOATDM>2.0.CO;2](https://doi.org/10.1175/1520-0493(1994)122<0671:DOATDM>2.0.CO;2).
- Hahn, L., C. C. Ummerhofer, and Y.-O. Kwon, 2018: North Atlantic natural variability modulates emergence of widespread Greenland melt in a warming climate. *Geophys. Res. Lett.*, **45**, 9171–9178, <https://doi.org/10.1029/2018GL079682>.
- Häkkinen, S., D. K. Hall, C. A. Shuman, D. L. Worthen, and N. E. Digirolamo, 2014: Greenland Ice Sheet melt from MODIS and associated atmospheric variability. *Geophys. Res. Lett.*, **41**, 1600–1607, <https://doi.org/10.1002/2013GL059185>.
- Hall, D. K., J. C. Comiso, N. E. Digirolamo, C. A. Shuman, J. E. Box, and L. S. Koenig, 2013: Variability in the surface temperature and melt extent of the Greenland Ice Sheet from MODIS. *Geophys. Res. Lett.*, **40**, 2114–2120, <https://doi.org/10.1002/grl.50240>.
- Hanna, E., and Coauthors, 2011: Greenland Ice Sheet surface mass balance 1870 to 2010 based on twentieth century reanalysis, and links with global climate forcing. *J. Geophys. Res.*, **116**, D24121, <https://doi.org/10.1029/2011JD016387>.
- , X. Fettweis, and R. J. Hall, 2018: Brief communication: Recent changes in summer Greenland blocking captured by none of the CMIP5 models. *Cryosphere*, **12**, 3287–3292, <https://doi.org/10.5194/tc-12-3287-2018>.
- , S. H. Mernild, J. Cappelen, and K. Steffen, 2012: Recent warming in Greenland in a long-term instrumental (1881–2012) climatic context: I. Evaluation of surface air temperature records. *Environ. Res. Lett.*, **7**, 045404, <https://doi.org/10.1088/1748-9326/7/4/045404>.
- , T. E. Cropper, R. J. Hall, and J. Cappelen, 2016: Greenland Blocking Index 1851–2015: A regional climate change signal. *Int. J. Climatol.*, **36**, 4847–4861, <https://doi.org/10.1002/joc.4673>.
- , J. M. Jones, J. Cappelen, S. H. Mernild, L. Wood, K. Steffen, and P. Huybrechts, 2013: The influence of North Atlantic atmospheric and oceanic forcing effects on 1900–2010 Greenland summer climate and ice melt/runoff. *Int. J. Climatol.*, **33**, 862–880, <https://doi.org/10.1002/joc.3475>.
- Harper, J., N. Humphrey, W. T. Pfeffer, J. Brown, and X. Fettweis, 2012: Greenland ice-sheet contribution to sea-level rise buffered by meltwater storage in firn. *Nature*, **491**, 240–243, <https://doi.org/10.1038/nature11566>.
- Hermann, M., L. Papritz, and H. Wernli, 2020: A Lagrangian analysis of the dynamical and thermodynamic drivers of large-scale Greenland melt events during 1979–2017. *Wea. Climate Dyn.*, **1**, 497–518, <https://doi.org/10.5194/wcd-1-497-2020>.
- Hersbach, H., and Coauthors, 2020: The ERA5 global reanalysis. *Quart. J. Roy. Meteor. Soc.*, **146**, 1999–2049, <https://doi.org/10.1002/qj.3803>.
- Hofer, S., A. J. Tedstone, X. Fettweis, and J. L. Bamber, 2017: Decreasing cloud cover drives the recent mass loss on the Greenland Ice Sheet. *Sci. Adv.*, **3**, e1700584, <https://doi.org/10.1126/sciadv.1700584>.
- How, P., and Coauthors, 2021: Greenland-wide inventory of ice marginal lakes using a multi-method approach. *Sci. Rep.*, **11**, 4481, <https://doi.org/10.1038/s41598-021-83509-1>.
- Howat, I. M., S. de la Peña, J. H. van Angelen, J. T. M. Lenaerts, and M. R. van den Broeke, 2013: Brief Communication “Expansion of meltwater lakes on the Greenland ice sheet”. *Cryosphere*, **7**, 201–204, <https://doi.org/10.5194/tc-7-201-2013>.
- Huai, B., M. R. Van den Broeke, and C. H. Reijmer, 2020: Long-term surface energy balance of the western Greenland Ice Sheet and the role of large-scale circulation variability. *Cryosphere*, **14**, 4181–4199, <https://doi.org/10.5194/tc-14-4181-2020>.
- IPCC, 2022: Summary for policymakers. *Climate Change 2022: Impacts, Adaptation and Vulnerability*, H. O. Pörtner et al., Eds., Cambridge University Press, 3–33.
- Kalnay, E., and Coauthors, 2018: The NCEP/NCAR 40-year reanalysis project. *Renewable Energy*, Vol. **I**, Routledge, 146–194.
- Keegan, K. M., M. R. Albert, J. R. McConnell, and I. Baker, 2014: Climate change and forest fires synergistically drive widespread melt events of the Greenland Ice Sheet. *Proc. Natl. Acad. Sci. USA*, **111**, 7964–7967.
- Kendall, M. G., 1949: Rank and product-moment correlation. *Biometrika*, **36**, 177–193, <https://doi.org/10.1093/biomet/36.1-2.177>.
- Kjeldsen, K. K., and Coauthors, 2015: Spatial and temporal distribution of mass loss from the Greenland Ice Sheet since AD 1900. *Nature*, **528**, 396–400, <https://doi.org/10.1038/nature16183>.
- Krasting, J. P., A. J. Broccoli, K. W. Dixon, and J. R. Lanzante, 2013: Future changes in Northern Hemisphere snowfall. *J. Climate*, **26**, 7813–7828, <https://doi.org/10.1175/JCLI-D-12-00832.1>.
- Lemus-Canovas, M., J. A. Lopez-Bustins, J. Martin-Vide, and D. Royé, 2019: synoptReg: An R package for computing a synoptic climate classification and a spatial regionalization of environmental data. *Environ. Model. Software*, **118**, 114–119, <https://doi.org/10.1016/j.envsoft.2019.04.006>.
- Lim, Y.-K., S. D. Schubert, S. M. J. Nowicki, J. N. Lee, A. M. Molod, R. I. Cullather, B. Zhao, and I. Velicogna, 2016: Atmospheric summer teleconnections and Greenland Ice Sheet surface mass variations: Insights from MERRA-2. *Environ. Res. Lett.*, **11**, 024002, <https://doi.org/10.1088/1748-9326/11/2/024002>.
- MacFerrin, M., and Coauthors, 2019: Rapid expansion of Greenland’s low-permeability ice slabs. *Nature*, **573**, 403–407, <https://doi.org/10.1038/s41586-019-1550-3>.
- Mattingly, K. S., C. A. Ramseyer, J. J. Rosen, T. L. Mote, and R. Muthyala, 2016: Increasing water vapor transport to the Greenland Ice Sheet revealed using self-organizing maps. *Geophys. Res. Lett.*, **43**, 9250–9258, <https://doi.org/10.1002/2016GL070424>.
- , T. L. Mote, and X. Fettweis, 2018: Atmospheric river impacts on Greenland Ice Sheet surface mass balance. *J. Geophys. Res.*, **123**, 8538–8560, <https://doi.org/10.1029/2018JD028714>.
- , —, —, D. Van As, K. Van Tricht, S. Lhermitte, C. Pettersen, and R. S. Fausto, 2020: Strong summer atmospheric rivers trigger Greenland Ice Sheet Melt through spatially varying surface energy balance and cloud regimes. *J. Climate*, **33**, 6809–6832, <https://doi.org/10.1175/JCLI-D-19-0835.1>.
- , J. V. Turton, J. D. Wille, B. Noël, X. Fettweis, Å. K. Rennermalm, and T. L. Mote, 2023: Increasing extreme melt in northeast Greenland linked to foehn winds and atmospheric rivers. *Nat. Commun.*, **14**, 1743, <https://doi.org/10.1038/s41467-023-37434-8>.
- McGrath, D., W. Colgan, N. Bayou, A. Muto, and K. Steffen, 2013: Recent warming at summit, Greenland: Global context and implications. *Geophys. Res. Lett.*, **40**, 2091–2096, <https://doi.org/10.1002/grl.50456>.
- McLeod, J. T., and T. L. Mote, 2016: Linking interannual variability in extreme Greenland blocking episodes to the recent increase in summer melting across the Greenland Ice Sheet. *Int. J. Climatol.*, **36**, 1484–1499, <https://doi.org/10.1002/joc.4440>.

- Mikkelsen, A. B., and Coauthors, 2016: Extraordinary runoff from the Greenland ice sheet in 2012 amplified by hypsometry and depleted firn retention. *Cryosphere*, **10**, 1147–1159, <https://doi.org/10.5194/tc-10-1147-2016>.
- Mioduszewski, J. R., A. K. Rennermalm, A. Hammann, M. Tedesco, E. U. Noble, J. C. Stroeve, and T. L. Mote, 2016: Atmospheric drivers of Greenland surface melt revealed by self-organizing maps. *J. Geophys. Res. Atmos.*, **121**, 5095–5114, <https://doi.org/10.1002/2015JD024550>.
- Mote, T. L., 1998: Mid-tropospheric circulation and surface melt on the Greenland Ice Sheet: I. Atmospheric teleconnections. *Int. J. Climatol.*, **18**, 111–129, [https://doi.org/10.1002/\(SICI\)1097-0088\(199802\)18:2<111::AID-JOC227>3.0.CO;2-X](https://doi.org/10.1002/(SICI)1097-0088(199802)18:2<111::AID-JOC227>3.0.CO;2-X).
- , 2007: Greenland surface melt trends 1973–2007: Evidence of a large increase in 2007. *Geophys. Res. Lett.*, **34**, L22507, <https://doi.org/10.1029/2007GL031976>.
- Mouginot, J., and Coauthors, 2019: Forty-six years of Greenland Ice Sheet mass balance from 1972 to 2018. *Proc. Natl. Acad. Sci. USA*, **116**, 9239–9244, <https://doi.org/10.1073/pnas.1904242116>.
- Mudryk, L., M. Santolaria-Otín, G. Krinner, M. Ménégoz, C. Derksen, C. Brutel-Vuilmet, M. Brady, and R. Essery, 2020: Historical Northern Hemisphere snow cover trends and projected changes in the CMIP6 multi-model ensemble. *Cryosphere*, **14**, 2495–2514, <https://doi.org/10.5194/tc-14-2495-2020>.
- Nghiem, S. V., and Coauthors, 2012: The extreme melt across the Greenland Ice Sheet in 2012. *Geophys. Res. Lett.*, **39**, L20502, <https://doi.org/10.1029/2012GL053611>.
- Niwano, M., A. Hashimoto, and T. Aoki, 2019: Cloud-driven modulations of Greenland Ice Sheet surface melt. *Sci. Rep.*, **9**, 10380, <https://doi.org/10.1038/s41598-019-46152-5>.
- Noël, B., W. J. Van de Berg, S. Lhermitte, and M. R. Van den Broeke, 2019: Rapid ablation zone expansion amplifies north Greenland mass loss. *Sci. Adv.*, **5**, eaav0123, <https://doi.org/10.1126/sciadv.aav0123>.
- Oltmanns, M., F. Straneo, and M. Tedesco, 2019: Increased Greenland melt triggered by large-scale, year-round cyclonic moisture intrusions. *Cryosphere*, **13**, 815–825, <https://doi.org/10.5194/tc-13-815-2019>.
- Orsi, A. J., and Coauthors, 2017: The recent warming trend in North Greenland. *Geophys. Res. Lett.*, **44**, 6235–6243, <https://doi.org/10.1002/2016GL072212>.
- Philipp, A., C. Beck, R. Huth, and J. Jacobeit, 2016: Development and comparison of circulation type classifications using the COST 733 dataset and software. *Int. J. Climatol.*, **36**, 2673–2691, <https://doi.org/10.1002/joc.3920>.
- Poinar, K., I. Joughin, S. B. Das, M. D. Behn, J. T. M. Lenaerts, and M. R. van den Broeke, 2015: Limits to future expansion of surface-melt-enhanced ice flow into the interior of western Greenland. *Geophys. Res. Lett.*, **42**, 1800–1807, <https://doi.org/10.1002/2015GL063192>.
- Preece, J. R., T. L. Mote, J. Cohen, L. J. Wachowicz, J. A. Knox, M. Tedesco, and G. J. Kooperman, 2023: Summer atmospheric circulation over Greenland in response to Arctic amplification and diminished spring snow cover. *Nat. Commun.*, **14**, 3759, <https://doi.org/10.1038/s41467-023-39466-6>.
- Pulliainen, J., and Coauthors, 2020: Patterns and trends of Northern Hemisphere snow mass from 1980 to 2018. *Nature*, **581**, 294–298, <https://doi.org/10.1038/s41586-020-2258-0>.
- Rahmstorf, S., J. E. Box, G. Feulner, M. E. Mann, A. Robinson, S. Rutherford, and E. J. Schaffernicht, 2015: Exceptional twentieth-century slowdown in Atlantic Ocean overturning circulation. *Nat. Climate Change*, **5**, 475–480, <https://doi.org/10.1038/nclimate2554>.
- Räisänen, J., 2008: Warmer climate: Less or more snow? *Climate Dyn.*, **30**, 307–319, <https://doi.org/10.1007/s00382-007-0289-y>.
- Rajewicz, J., and S. J. Marshall, 2014: Variability and trends in anticyclonic circulation over the Greenland Ice Sheet, 1948–2013. *Geophys. Res. Lett.*, **41**, 2842–2850, <https://doi.org/10.1002/2014GL059255>.
- Rantanen, M., A. Y. Karpechko, A. Lipponen, K. Nordling, O. Hyvärinen, K. Ruosteenoja, T. Vihma, and A. Laaksonen, 2022: The Arctic has warmed nearly four times faster than the globe since 1979. *Commun. Earth Environ.*, **3**, 168, <https://doi.org/10.1038/s43247-022-00498-3>.
- Rignot, E., and J. Mouginot, 2012: Ice flow in Greenland for the international polar year 2008–2009. *Geophys. Res. Lett.*, **39**, L11501, <https://doi.org/10.1029/2012GL051634>.
- Ryan, J. C., L. C. Smith, D. Van As, S. W. Cooley, M. G. Cooper, L. H. Pitcher, and A. Hubbard, 2019: Greenland Ice Sheet surface melt amplified by snowline migration and bare ice exposure. *Sci. Adv.*, **5**, eaav3738, <https://doi.org/10.1126/sciadv.aav3738>.
- Sen, P. K., 1968: Estimates of the regression coefficient based on Kendall's tau. *J. Amer. Stat. Assoc.*, **63**, 1379–1389, <https://doi.org/10.1080/01621459.1968.10480934>.
- Serreze, M. C., and R. G. Barry, 2011: Processes and impacts of Arctic amplification: A research synthesis. *Global Planet. Change*, **77**, 85–96, <https://doi.org/10.1016/j.gloplacha.2011.03.004>.
- Slater, T., and Coauthors, 2021: Increased variability in Greenland Ice Sheet runoff from satellite observations. *Nat. Commun.*, **12**, 6069, <https://doi.org/10.1038/s41467-021-26229-4>.
- Tedesco, M., M. Serreze, and X. Fettweis, 2008: Diagnosing the extreme surface melt event over southwestern Greenland in 2007. *Cryosphere*, **2**, 159–166, <https://doi.org/10.5194/tc-2-159-2008>.
- , and X. Fettweis, 2020: Unprecedented atmospheric conditions (1948–2019) drive the 2019 exceptional melting season over the Greenland Ice Sheet. *Cryosphere*, **14**, 1209–1223, <https://doi.org/10.5194/tc-14-1209-2020>.
- , T. Mote, X. Fettweis, E. Hanna, J. Jeyaratnam, J. F. Booth, R. Datta, and K. Briggs, 2016: Arctic cut-off high drives the poleward shift of a new Greenland melting record. *Nat. Commun.*, **7**, 11723, <https://doi.org/10.1038/ncomms11723>.
- , X. Fettweis, M. R. Van den Broeke, R. S. W. Van de Wal, C. J. P. P. Smeets, W. J. Van de Berg, M. C. Serreze, and J. E. Box, 2011: The role of albedo and accumulation in the 2010 melting record in Greenland. *Environ. Res. Lett.*, **6**, 014005, <https://doi.org/10.1088/1748-9326/6/1/014005>.
- , —, T. Mote, J. Wahr, P. Alexander, J. E. Box, and B. Wouters, 2013: Evidence and analysis of 2012 Greenland records from spaceborne observations, a regional climate model and reanalysis data. *Cryosphere*, **7**, 615–630, <https://doi.org/10.5194/tc-7-615-2013>.
- Välisuo, I., T. Vihma, R. Pirazzini, and M. Schäfer, 2018: Interannual variability of atmospheric conditions and surface melt in Greenland in 2000–2014. *J. Geophys. Res. Atmos.*, **123**, 10 443–10 463, <https://doi.org/10.1029/2018JD028445>.
- van den Broeke, M., P. Smeets, J. Ettema, C. Van der Veen, R. Van de Wal, and J. Oerlemans, 2008: Partitioning of melt energy and meltwater fluxes in the ablation zone of the west Greenland Ice Sheet. *Cryosphere*, **2**, 179–189, <https://doi.org/10.5194/tc-2-179-2008>.

- Van Tricht, K., and Coauthors, 2016: Clouds enhance Greenland Ice Sheet meltwater runoff. *Nat. Commun.*, **7**, 10266, <https://doi.org/10.1038/ncomms10266>.
- Vizcaíno, M., W. H. Lipscomb, W. J. Sacks, and M. van den Broeke, 2014: Greenland surface mass balance as simulated by the community earth system model. Part II: Twenty-first-century changes. *J. Climate*, **27**, 215–226, <https://doi.org/10.1175/JCLI-D-12-00588.1>.
- Ward, J. L., M. G. Flanner, and E. Dunn-Sigouin, 2020: Impacts of Greenland block location on clouds and surface energy fluxes over the Greenland Ice Sheet. *J. Geophys. Res. Atmos.*, **125**, e2020JD033172, <https://doi.org/10.1029/2020JD033172>.
- Wei, T., B. Noël, M. Ding, and Q. Yan, 2022: Spatiotemporal variations of extreme events in surface mass balance over Greenland during 1958–2019. *Int. J. Climatol.*, **42**, 8008–8023, <https://doi.org/10.1002/joc.7689>.
- Williamson, C. J., and Coauthors, 2020: Algal photophysiology drives darkening and melt of the Greenland Ice Sheet. *Proc. Natl. Acad. Sci. USA*, **117**, 5694–5705, <https://doi.org/10.1073/pnas.1918412117>.
- Wilton, D. J., A. Jowett, E. Hanna, G. R. Bigg, M. R. Van den Broeke, X. Fettweis, and P. Huybrechts, 2017: High resolution (1 km) positive degree-day modelling of Greenland Ice Sheet surface mass balance, 1870–2012 using reanalysis data. *J. Glaciol.*, **63**, 176–193, <https://doi.org/10.1017/jog.2016.133>.